

Milliarcsec-scale radio structure of a matched sample of Seyfert 1 and Seyfert 2 galaxies^{★,★★}

D. V. Lal^{1,2,***}, P. Shastri¹, and D. C. Gabuzda³

¹ Indian Institute of Astrophysics, Koramangala, Bangalore – 560 034, India
e-mail: dharam@ncra.tifr.res.in

² Department of Physics, Indian Institute of Science, Bangalore – 560 012, India

³ Department of Physics, University College Cork, Cork, Republic of Ireland

Received ; accepted

Abstract. We have obtained mas-scale resolution very long baseline interferometry (VLBI) images of a sample of Seyfert 1 and Seyfert 2 galaxies at 5 GHz (wavelength, $\lambda = 6$ cm). The Seyferts of the two types were chosen to be matched in several orientation-independent properties, primarily in order to rigorously test predictions of the unified scheme. We detected all the 15 objects that we observed. In this paper we describe the observations and data reduction procedures, and present the VLBI radio images as well as simultaneous Very Large Array images that we obtained for these 15 Seyferts.

Key words. Seyfert – radio continuum: galaxies

1. Introduction

Seyfert galaxies have been long-recognized as a class of active galactic nuclei (AGN) that are at the low end of the luminosity range (and the distance range) of AGN, and primarily characterized by optical emission lines that have a wide range of ionization (*e.g.*, Osterbrock 1989). Usually the term “Seyfert galaxy” is used to refer to radio-quiet AGN that are in spiral host galaxies. The current majority-view is that the nuclei of Seyfert galaxies are powered by super-massive black holes, although there is also the alternate view that star bursts *alone* can power Seyferts (*e.g.*, Cid Fernandes (1997) and refs therein).

Khachikian & Weedman (1974) identified two types of Seyfert galaxies on the basis of the widths of the nuclear emission lines. While spectra of type 2 Seyfert galaxies have relatively narrow emission lines (FWHM ≈ 300 km s⁻¹ to 1000 km s⁻¹), the hydrogen and helium lines in the spectra of type 1 Seyfert galaxies have an additional much broader component (FWHM ≥ 1000 km s⁻¹). The Unified Scheme (US) for Seyfert galaxies (*e.g.*, Antonucci 1993) hypothesizes that Seyfert 1s and 2s constitute the same parent population and appear different *solely* due to their differing orientations. The

US requires the presence of optically thick material around the central region in the form of a torus (*e.g.*, Pier & Krolik 1993). When the torus is face-on, the broad emission lines from the central clouds are directly visible, as in Seyfert 1s, whereas when the torus is edge-on, it obscures these clouds from view, resulting in Seyfert 2s. The US found particularly strong support in the discovery of *polarized* broad emission lines from Seyfert 2s (Antonucci & Miller (1985); Moran et al. (2000)), which are interpreted as originating from the hidden clouds but scattered periscopically into our line of sight.

The US has definite predictions for the radio morphology of Seyferts: the total radio luminosities of Seyfert 1s and 2s are expected to be similar and the radio structures are expected to differ only by projection effects. Indeed, Seyfert 1s and 2s have been shown to have similar luminosities on various spatial scales (Ulvestad & Wilson 1989). The result of Roy et al. (1994), however, contradicts the US. They reported that Seyfert 2s, *i.e.*, those that have edge-on tori in the US, have a larger likelihood of showing compact radio emission than Seyfert 1s. On the other hand, the simple US predicts that there should be no such difference between the Seyfert sub-classes.

The intriguing result of Roy et al. was obtained using relatively large samples of Seyferts, but the compact structure was measured using a 275 km interferometer between the Parkes and Tidbinbilla telescopes. We sought to improve upon their experiment by using pc-scale, *i.e.*, Very Long Baseline Interferometry (VLBI) *images* of Seyferts rather than a single-baseline measurement of the visibility and by designing our sample so as to enable *rigorous* tests of the US. Our sample

Send offprint requests to: Dharam Vir Lal

* The other 24 panels of Fig. 1 are only available in electronic form. The full paper copies can be obtained from the authors.

** Tables 3–4 are only available in electronic form and Tables 5–6 are also available at the CDS via anonymous ftp to cdsarc.u-strasbg.fr (130.79.128.5) or via <http://cdsweb.u-strasbg.fr/cgi-bin/qcat?J/A+A/>

*** Present address: National Centre for Radio Astrophysics, Post Bag 3, Ganeshkhind, Pune 411 007, India

selection is described in detail in an accompanying paper. The key point is that the Seyfert 1s and Seyfert 2s were chosen to be *matched* in a range of orientation-independent properties, so that we can compare objects of the two types that should be *intrinsically similar* in the framework of the US.

Our sample has 10 Seyfert 1s and 10 Seyfert 2s, including 15 objects that did not have prior VLBI observations. We present here images derived from global VLBI and simultaneous Very Large Array (VLA) observations of these 15 objects at 5 GHz. In a later paper, when interpreting our results, we will combine our data with previously published data for the remaining five objects of our sample (see also Shastri *et al.* (2003)).

2. Observations

We obtained global VLBI observations of the 15 Seyfert galaxies (see Table 1) in our sample that did not have prior VLBI observations published in the literature during a single 24 hour run on February 18, 1998. Since the phased VLA was one of our VLBI stations, we also obtained simultaneous VLA aperture-synthesis data for all these 15 sources.

2.1. VLBI observations

The global VLBI array consisted of a total of 14 stations: three stations of the European VLBI Network (EVN), *viz.*, Effelsberg (Germany), Torun (Poland) and Noto (Italy), all 10 stations of the Very Long Baseline Array (VLBA) and the phased VLA. The inclusion of two stations with relatively large collecting area, *viz.*, Effelsberg and the phased VLA, was critical to our ability to detect the radio-faint Seyferts in our sample. Information about the global VLBI observations is summarized in Table 2.

Short observations of four compact bright sources, *viz.*, 3C 84, 3C 345, DA 193, and 4C 39.25 were included in the VLBI schedule as ‘fringe finders’, *i.e.*, strong sources intended to provide checks of the basic parameters of the experiment, such as the set-up at each station, station coordinates, source coordinates, etc.

Our Seyfert galaxy targets were too weak to be used to phase the VLA array. Therefore, we phased the VLA with observations of sources from the VLA calibrator list located near the targets just prior to each VLBI scan. Since the VLA was not typically the slowest slewing antenna in the array, it was usually possible to phase the VLA while the slower antennas were still slewing, minimizing the need to extend the phasing time into the start of the VLBI scans. These phasing sources also served as VLA phase calibrators during the calibration of VLA observations in aperture-synthesis mode; see Sect. 2.2.

We observed our targets in snap-shot mode, sequencing them in order to (i) roughly equalize the number of scans for the various targets, (ii) optimize the (u, v) coverage for each target and (iii) include as many stations as possible in as many scans as possible for each target. We used the SCHED software from NRAO (Walker 2003) to create the schedule of observations. The duration of each scan was 8 min 48 s, and the number of scans per target ranged between 7 and 12.

2.2. VLA observations

During all of the VLBI scans in which the VLA participated, simultaneous VLA data for the target in aperture-synthesis mode were also acquired. This resulted in simultaneous arcsec-scale data for all our targets. The calibrators used to phase the VLA prior to the VLBI scans were chosen to be ‘P’ (unresolved) or ‘S’ (slightly resolved) calibrators close to the targets. As is noted above, these phase calibrators (listed in Table 3) served the dual purpose of phasing the VLA for the VLBI observations and acting as phase calibrators for the aperture-synthesis-mode VLA data. Typically, about 8.5 min of aperture-synthesis mode VLA data were obtained for the target during each scan, as well as ~ 2 min on the corresponding phase calibrator prior to each scan. The centre wavelength and bandwidth of the observations are the same as that of the VLBI observations.

3. Data reduction

3.1. VLBI data

The data recorded at each station were correlated at the VLBA correlator at NRAO, Socorro. The correlated data were reduced in the standard way using the NRAO Astronomical Image Processing System (AIPS) package. The amplitude calibration for all antennas except for the VLA was carried out using gain curves supplied by each station and system temperatures measured before or during scan in each baseband channel. The amplitudes for baselines involving the VLA were calibrated using flux densities for the targets determined from the VLA data in aperture-synthesis mode together with ratios of the VLA source-to-system temperature measured during the observations. The resulting errors in the visibility amplitudes are about 5 % or less, as indicated by the data for the compact fringe-finder DA 193 (whose flux density was 5.38 Jy).

The phases in the eight baseband channels were aligned by using the AIPS task FRING to solve for the phases and delays for a short observation of one of the fringe-finders and applying these solutions to the data for all sources (so-called ‘manual phase calibration’). FRING was then used to solve for small residual phase and delays for all the target scans, using the full bandwidth provided by the eight baseband channels to improve the signal-to-noise ratio for the solutions.

Before imaging, the data were averaged over the entire frequency bandwidth, then over time (with an averaging time of 30 s). During the iterative imaging procedure, the antenna gains were self-calibrated along with the source structure (hybrid mapping). We were able to iteratively self-calibrate only the phases for all the targets; our attempts at amplitude self-calibration failed due to the weakness of the targets and the wide range of baseline sensitivities in the inhomogeneous array. The phased VLA was used as the reference antenna in all cases, and uniform weighting was used in order to maximize the angular resolution of the images. The r.m.s. noise levels in the final images after completion of the self-calibration process were $0.09 \text{ mJy beam}^{-1}$ to $0.23 \text{ mJy beam}^{-1}$ (Table 4).

We model-fit the final self-calibrated data using the Brandeis package (Gabuzda 1988), which fits the data in the visibility domain. This avoids the need to account for the effect

Table 1. Seyfert galaxies that were observed using global VLBI. References for the optical positions: *a*: Clements (1981); *b*: Clements (1983); *c*: Argyle & Eldridge (1990); *d*: Gallouët *et al.* (1975). We use $H_0 = 75 \text{ km s}^{-1} \text{ Mpc}^{-1}$ and $q_0 = 0$.

Object	Position of optical nucleus		Redshift	Distance (Mpc)	Image scale (pc mas ⁻¹)
	Right Ascension (J2000)	Declination			
Mrk 1	01 ^h 16 ^m 07 ^s .25	+33°05′22″.40 ^a	0.016	63.5	0.31
MCG 8-11-11	05 ^h 54 ^m 53 ^s .61	+46°26′21″.61 ^a	0.025	98.8	0.48
NGC 2273	06 ^h 50 ^m 08 ^s .72	+60°50′45″.01 ^c	0.006	23.9	0.12
Mrk 78	07 ^h 42 ^m 41 ^s .73	+65°10′37″.46 ^a	0.037	145.4	0.69
Mrk 1218	08 ^h 38 ^m 10 ^s .95	+24°53′42″.92 ^b	0.029	114.4	0.55
NGC 2639	08 ^h 43 ^m 38 ^s .00	+50°12′20″.32 ^c	0.011	43.8	0.21
Mrk 766	12 ^h 18 ^m 26 ^s .51	+29°48′46″.34 ^a	0.013	51.7	0.25
Mrk 477	14 ^h 40 ^m 38 ^s .11	+53°30′16″.00 ^a	0.038	149.2	0.73
NGC 5929	15 ^h 26 ^m 06 ^s .13	+41°40′14″.72 ^b	0.009	35.8	0.18
NGC 7212	22 ^h 07 ^m 02 ^s .01	+10°14′00″.34 ^b	0.027	106.6	0.51
Ark 564	22 ^h 42 ^m 39 ^s .34	+29°43′31″.31 ^a	0.024	94.9	0.46
NGC 7469	23 ^h 03 ^m 15 ^s .62	+08°52′26″.39 ^a	0.016	63.5	0.31
Mrk 530	23 ^h 18 ^m 56 ^s .62	+00°14′38″.23 ^a	0.030	118.3	0.57
Mrk 533	23 ^h 27 ^m 56 ^s .72	+08°46′44″.53 ^b	0.029	114.4	0.55
NGC 7682	23 ^h 29 ^m 03 ^s .93	+03°31′59″.99 ^b	0.017	67.4	0.33

Table 2. Parameters of the VLBI observations.

Observing date	: February 18, 1998
Stations	: 10-element VLBA, Phased VLA, Effelsberg, Noto and Torun
Frequency	: 4964.474 MHz
Bandwidth	: 64 MHz
Polarization	: LCP only
Scan length	: 8 min 48 s
Aggregate bit rate	: 128 Mbit s ⁻¹ (8 baseband channels at 16 MSamples s ⁻¹ of 1 bit samples)
Fringe Finders	: 3C 84, 3C 345, DA 193, and 4C 39.25
Correlator	: NRAO, Socorro, NM, USA

of convolution with the synthesized beam in the image. The distribution of clean components was used to arrive at an initial “seed” model with up to five components (circular Gaussians or point sources), with each component corresponding to one cluster of CLEAN components. The components that emerged with significant emission as a result of the first iteration of the model-fitting procedure were retained and fed into a second iteration in order to arrive at the final result. The results are listed in Table 5.

We also list the total VLBI flux densities derived from the data in the image plane using the AIPS task IMEAN. (The task JMFIT, which fits two-dimensional Gaussians to components in the image plane gives very similar results to IMEAN in cases when there are no weak multiple components.) In the case of objects with significant extended emission, the flux density accounted for by model-fitting the visibilities turns out to be somewhat less than that obtained from the image, but the models contained > 80 % of the total flux density in but a few sources (see notes on individual sources below).

3.2. VLA data

The VLA data acquired in aperture-synthesis mode were processed in the standard way using AIPS. 1331+305 (3C 286) was used as the primary flux density calibrator. The VLA images were obtained using uniform weighting. The sources were subjected to several cycles of self-calibration, until the r.m.s. noise approached the thermal noise levels. The typical 1σ noise levels in the maps are in the range $30 \mu\text{Jy beam}^{-1}$ to $120 \mu\text{Jy beam}^{-1}$. We used data only from the first IF channel (*i.e.*, only half the total bandwidth), as the second IF channel suffered from unacceptably high noise levels. For each image, the flux densities of the components that were easily separable from neighbouring components or extensions were derived by fitting the data in the image plane with two-dimensional Gaussians using the AIPS task JMFIT. Thus diffuse extensions/components were left out of these estimates. The total flux density detected was estimated by summing all the flux density in a specified rectangular region using the AIPS task IMEAN. The total errors in the flux densities are typically 5 %, arising from the calibration and the r.m.s. noise.

4. Results

4.1. The radio images

The VLBI and VLA contour maps for all the targets are shown in Fig. 1. The sequence of maps is ordered in right ascension. The spatial coordinates for the VLA maps are given in absolute units, whereas coordinates for the VLBI maps are given relative to the phase centre, since absolute position information was lost during the self-calibration. An ellipse in a box in the lower left-hand corner of each map shows the shape of the synthesized beam FWHM. A cross in each of the VLA maps marks the position of the optical nucleus, with the size of the cross representing the uncertainty in the position. The optical positions are from Gallouët *et al.* (1975), Clements (1981, 1983), and Argyle & Eldridge (1990). Gallouët *et al.* (1975) quote typical position errors of 6 arcsec, and errors of 0.09 arcsec to 0.2 arcsec are given by the other authors. All positions are given in J2000 coordinates.

The beam FWHM, beam position angle, peak surface brightness, r.m.s. noise level and contour levels for all the maps are shown in Table 3 (VLA maps) and Table 4 (VLBI maps). The r.m.s. noise level (1σ) in the images was estimated using regions that were free of source emission using the AIPS task IMEAN. The r.m.s. noise of an empty region was then fed into a second iteration of IMEAN for the entire image, to obtain the r.m.s. deviation from a fit to the Gaussian (noise) part of the pixel histogram for the whole image.

Table 5 summarizes the VLBI observational results. It gives the object name, *a priori* coordinates used for the VLBI observations and for correlation of the interferometric data, peak surface brightness, components sizes, the total (summed) flux density for the model components and the total flux density in the image obtained using the AIPS task IMEAN.

The results of the VLA imaging are summarized in Table 6, which gives the object name, radio position of each component, offset of radio position from optical position, peak surface brightness, total flux density of each component, and the largest angular size of the source. The component flux densities were derived by model-fitting Gaussians in the image plane to those components that were easily separable from neighbouring components or extensions using the AIPS task JMFIT. For multiple components the corresponding parameters are given in separate rows of Table 6. The total flux density is that in a rectangular region enclosing all of the detected emission, derived using the AIPS task IMEAN in every case. The model-fitting procedure does not account for all the extended emission since only Gaussian components were used, and therefore the sum of the component flux densities is often lower than the total flux density. The largest angular size for each source is the size of the contour corresponding to 5 % of the peak surface brightness in the case of extended sources, which, in all cases is well above the noise in the image. For the unresolved sources, the FWHM of the major axis of the synthesized beam is listed as the upper limit.

4.2. Description of the sources

We describe here the arcsec-scale radio structure measured by the VLA (subsection “Y”) and the mas-scale structure derived from the global VLBI observations (subsection “G”) for each of the Seyfert galaxies. We also present two-frequency spectral indices, α , when measurements for other frequencies with similar resolution (≈ 1 arcsec) were available in the literature (the spectral index is defined as $S_\nu \propto \nu^{-\alpha}$).

Variability of the sources and differing angular resolutions for the images used can cause large uncertainties in the calculated spectral indices; we have accordingly attempted to use data that were obtained as near in time as possible to ours, and with angular resolution as close as possible to ours when calculating the spectral indices.

Mrk 1 (0113+328)

Y: Mrk 1 is unresolved. The total flux density is similar to that presented by Ulvestad *et al.* (1981) and is less than the value of 38 mJy found by Sramek & Tovmassian (1975). Ulvestad *et al.* (1981) suggest that, along with an unresolved component, there is a faint (~ 2 mJy) extension ~ 0.4 arcsec to the south. This faint extension is not detected in our map. Since Ulvestad *et al.* (1981) do not show a map for this source, it is difficult to judge whether we should have detected it. The peak radio surface brightness in our map is displaced ~ 1 arcsec to the south-west of the optical nucleus (Clements 1981).

G: The image shows only a single somewhat resolved component. Kukula *et al.* (1999) detected a compact radio central component surrounded by a halo of emission approximately 100 mas across at 1.7 GHz using the EVN (angular resolution ~ 20 mas). They find evidence for weak emission extending to the south, possibly leading into the larger structure (Ulvestad *et al.* 1981). However, they do not find any evidence for linear structure on scales larger than a few parsec. Our best model contains about 64 % of the total flux density on VLBI scales. The maximum extent of the source in our image is ~ 30 pc across.

MCG 8–11–11 (0551+464)

Y: Our map shows a strong nuclear component with a compact elongation extending toward the north-west (P.A. -45°). There is also larger-scale extended emission towards the north. The bright central component is coincident with the optical nucleus (Clements 1981), and the total extent of the north-south structure is ~ 3 arcsec. The radio image of Schmitt *et al.* (2001) at 8.4 GHz (VLA A array) is similar to ours. The 15 GHz map of Ulvestad & Wilson (1986) resolves the central component into a triple structure. The largest angular size of the source is ~ 3.5 arcsec.

G: The image shows a single somewhat resolved component. The weak component to the south-west (if real) has a flux density of ~ 0.6 mJy. Our best model contains about 63 % of the total flux density on VLBI scales.

NGC 2273 (0645+609)

Table 3. VLA phase calibrators and the parameters pertaining to the VLA maps.

Object	Phase calibrator	CLEAN beam		Peak (mJy beam ⁻¹)	Image r.m.s. (μ Jy beam ⁻¹)	Contours (% of peak surface brightness)
		(arcsec ²)	P.A. (deg)			
Mrk 1	0119+321	0.65 × 0.49	54.0	24.08	35	-0.3, 0.8, 1, 2, 4, 6, 8, 10, 12, 16, 24, 32, 40, 48, 56, 64, 80, 90
MCG 8-11-11	0604+442	0.84 × 0.44	57.7	23.57	52	-0.6, 0.6, 1, 2, 4, 6, 8, 10, 12, 16, 24, 32, 40, 48, 56, 64, 80, 90
NGC 2273	0650+600	0.70 × 0.46	60.2	12.13	85	-1.6, 1.6, 2, 4, 6, 8, 10, 12, 16, 24, 32, 40, 48, 56, 64, 80, 90
Mrk 78	0737+596	0.70 × 0.52	71.6	8.87	30	-1, 1, 1.6, 2, 4, 6, 8, 10, 12, 16, 24, 32, 40, 48, 56, 64, 80, 90
Mrk 1218	0837+249	0.53 × 0.41	-68.3	18.72	121	-1.2, 1.2, 2, 4, 6, 8, 10, 12, 16, 24, 32, 40, 48, 56, 64, 80, 90
NGC 2639	0832+492	0.64 × 0.45	81.6	63.47	70	-0.4, 0.4, 1, 2, 4, 6, 8, 10, 12, 16, 24, 32, 40, 48, 56, 64, 80, 90
Mrk 766	1217+301	0.65 × 0.48	-71.9	13.75	35	-0.8, 1, 2, 4, 6, 8, 10, 12, 16, 24, 32, 40, 48, 56, 64, 80, 90
Mrk 477	1419+543	0.99 × 0.55	-63.3	22.97	34	-0.3, 0.8, 1, 2, 4, 6, 8, 10, 12, 16, 24, 32, 40, 48, 56, 64, 80, 90
NGC 5929	1458+373	1.16 × 0.98	75.4	21.51	95	-0.8, 1.6, 2, 4, 6, 8, 10, 12, 16, 24, 32, 40, 48, 56, 64, 80, 90
NGC 7212	2151+071	1.18 × 0.68	-65.1	19.59	77	-0.8, 0.8, 1, 2, 4, 6, 8, 10, 12, 16, 24, 32, 40, 48, 56, 64, 80, 90
Ark 564	2236+284	0.85 × 0.75	8.4	8.62	40	-1.6, 1.6, 2, 4, 6, 8, 10, 12, 16, 24, 32, 40, 48, 56, 64, 80, 90
NGC 7469	2257+077	0.61 × 0.55	54.9	21.97	49	-0.6, 0.6, 1, 2, 4, 6, 8, 10, 12, 16, 24, 32, 40, 48, 56, 64, 80, 90
Mrk 530	2323-032	0.82 × 0.53	35.2	8.02	41	-1.6, 1.6, 2, 4, 6, 8, 10, 12, 16, 24, 32, 40, 48, 56, 64, 80, 90
Mrk 533	2330+110	0.82 × 0.53	35.2	38.19	72	-0.4, 0.4, 1, 2, 4, 8, 15, 24, 32, 40, 48, 56, 64, 72, 80, 90
NGC 7682	2330+110	0.94 × 0.64	38.2	21.98	36	-0.4, 0.6, 1, 2, 4, 6, 8, 10, 12, 16, 24, 32, 40, 48, 56, 64, 80, 90

Table 4. Contour levels and other parameters for VLBI maps. ★: Some scans did not include all the stations of the global array.

Object	No. of scans★	CLEAN beam		Peak (mJy beam ⁻¹)	Image r.m.s. (μ Jy beam ⁻¹)	Contours (% of peak surface brightness)
		(mas ²)	P.A. (deg)			
Mrk 1	13	3.69 × 1.78	-12.2	6.7	135	-6, 8, 10, 12, 16, 24, 32, 40, 48, 56, 64, 80, 90
MCG 8-11-11	13	2.08 × 1.60	-53.9	6.9	121	-8, 8, 10, 12, 16, 24, 32, 40, 48, 56, 64, 80, 90
NGC 2273	11	3.02 × 2.52	28.1	7.5	131	-6, 8, 10, 12, 16, 24, 32, 40, 48, 56, 64, 80, 90
Mrk 78	18	3.61 × 2.43	85.0	7.1	145	-8, 8, 10, 12, 16, 24, 32, 40, 48, 56, 64, 80, 90
Mrk 1218	7	2.88 × 1.05	-10.4	6.7	110	-5, 6, 8, 10, 12, 16, 24, 32, 40, 48, 56, 64, 80, 90
NGC 2639	12	1.82 × 1.08	-6.8	34.8	85	-0.5, 0.5, 1, 2, 4, 8, 16, 24, 32, 40, 48, 56, 64, 72, 80, 90
Mrk 766	11	2.78 × 1.65	18.3	7.1	131	-8, 8, 10, 12, 16, 24, 32, 40, 48, 56, 64, 80, 90
Mrk 477	10	4.48 × 3.26	50.0	9.4	144	-4, 4, 6, 8, 10, 12, 16, 24, 32, 40, 48, 56, 64, 80, 90
NGC 5929	11	2.91 × 1.80	31.5	6.9	120	-6, 8, 10, 12, 16, 24, 32, 40, 48, 56, 64, 80, 90
NGC 7212	7	4.27 × 2.65	-3.5	7.2	233	-8, 8, 10, 12, 16, 24, 32, 40, 48, 56, 64, 80, 90
Ark 564	11	2.54 × 1.25	13.0	3.7	91	-16, 12, 16, 24, 32, 40, 48, 56, 64, 80, 90
NGC 7469	7	3.65 × 2.67	2.7	7.4	146	-8, 8, 10, 12, 16, 24, 32, 40, 48, 56, 64, 80, 90
Mrk 530	7	3.93 × 2.54	-4.8	8.8	132	-6, 6, 8, 10, 12, 16, 24, 32, 40, 48, 56, 64, 80, 90
Mrk 533	7	6.22 × 3.89	-4.2	10.2	117	-4, 4, 6, 8, 10, 12, 16, 24, 32, 40, 48, 56, 64, 80, 90
NGC 7682	7	4.00 × 3.00	1.9	8.9	149	-6, 8, 10, 12, 16, 24, 32, 40, 48, 56, 64, 80, 90

Y: Our map has similar features to those seen previously by Nagar *et al.* (1999) at 8.4 GHz and Ulvestad & Wilson (1984a) at 5 GHz. The source consists of an unequal double with a separation of nearly 1 arcsec in P.A. $\sim -80^\circ$. The WSRT image of this source at 5 GHz reported by Baum *et al.* (1993) shows amorphous structure on larger scales (> 2.5 arcsec). Our central-component flux density and total flux density are slightly higher than those in the 5 GHz image of Ulvestad & Wilson (1984b) with a similar

resolution. The optical nucleus (Argyle & Eldridge 1990) is ~ 0.6 arcsec to the east of the peak radio surface brightness.

G: The image shows a single somewhat resolved component. There is some evidence from the distribution of CLEAN components for possible weak emission out to ~ 1 mas from the phase centre.

Mrk 78 (0737+652)

Table 5. The VLBI results. †: See description of the Seyfert in Sect. 4.2.

Object	<i>a priori</i> position used for the correlation		Peak surface brightness (mJy beam ⁻¹)	Model-fit components					Total flux density from the image (mJy)
	Right Ascension (J2000)	Declination		Position relative to phase centre		FWHM (mas)	Flux density (mJy)	Total (mJy)	
				α (mas)	δ (mas)				
Mrk 1	01 ^h 16 ^m 07 ^s .22	+33°05'21".6	6.7	+0.0	+0.0	1.0	4.4	4.4	6.9
MGC 8-11-11	05 ^h 54 ^m 53 ^s .61	+46°26'21".7	6.9	+0.0	+0.0	0.8	4.9	4.9	7.8
NGC 2273	06 ^h 50 ^m 08 ^s .64	+60°50'44".9	7.5	+0.0	-0.1	1.2	6.3	6.3	7.7
Mrk 78	07 ^h 42 ^m 41 ^s .74	+65°10'37".8	7.1	+0.0	+0.1	0.7	5.2	8.5	9.0
				-0.7	+0.1	0.2	1.4		
				-1.5	-2.0	0.6	1.0		
				+0.8	-3.4	0.2	0.3		
				+3.7	+5.3	0.6	0.6		
Mrk 1218	08 ^h 38 ^m 10 ^s .95	+24°53'42".9	6.7	+0.0	+0.0	1.1	7.0	12.3 [†]	14.8
				+0.1	-5.9	2.8	1.7		
				-1.8	+4.3	2.1	2.8		
				+6.5	-5.3	0.9	0.8		
NGC 2639	08 ^h 43 ^m 38 ^s .07	+50°12'20".1	34.8	+0.0	+0.0	0.1	31.6	39.5	40.2
				+0.5	-0.1	0.3	8.0		
Mrk 766	12 ^h 18 ^m 26 ^s .52	+29°48'46".5	7.1	+0.0	+0.0	0.9	3.7	3.6	6.3
Mrk 477	14 ^h 40 ^m 38 ^s .10	+53°30'16".1	9.4	+0.3	+0.0	1.4	8.2	8.1	10.3
NGC 5929	15 ^h 26 ^m 06 ^s .17	+41°40'14".4	6.9	+0.0	-0.2	0.8	6.0	6.2	7.2
				+3.8	+2.1	0.2	0.3		
NGC 7212	22 ^h 07 ^m 02 ^s .06	+10°14'02".6	7.2	+0.0	-0.1	1.1	6.5	7.0	7.9
				-5.0	-1.0	1.1	0.5		
Ark 564	22 ^h 42 ^m 39 ^s .36	+29°43'30".9	3.7	+0.2	-0.1	0.9	3.2	3.2 [†]	9.1
NGC 7469	23 ^h 03 ^m 15 ^s .62	+08°52'26".1	7.4	+0.1	-0.1	0.9	5.5	6.1	7.4
				+0.0	-4.5	0.1	0.7		
Mrk 530	23 ^h 18 ^m 56 ^s .65	+00°14'38".0	8.8	+0.0	+0.5	0.9	7.6	8.6	9.7
				-1.3	-1.4	0.1	0.3		
				+3.4	-1.1	0.9	0.8		
Mrk 533	23 ^h 27 ^m 56 ^s .71	+08°46'44".1	10.2	+0.1	-0.1	1.1	9.7	16.9	20.5
				+6.2	-2.0	0.7	2.2		
				+16.7	-4.0	0.5	1.2		
				-6.0	+0.4	2.2	2.3		
				-13.8	-0.3	0.8	1.6		
NGC 7682	23 ^h 29 ^m 03 ^s .92	+03°31'59".9	8.9	+0.1	-0.3	0.9	7.6	11.5 [†]	14.2
				+3.2	-2.5	Point	2.1		
				-0.1	-5.5	Point	1.8		

Y: Mrk 78 is an extended source nearly 4 arcsec in size in our 5 GHz image. The bright central component is resolved and is coincident with the optical nucleus (Clements 1981). The secondary component is nearly 2 arcsec to the west of the main peak (P.A. $\sim -90^\circ$). The brighter component is also extended roughly in the east-west direction (P.A. $\sim 80^\circ$).

G: Our map shows a faint extension towards the south-west (P.A. $\sim -130^\circ$). Model-fitting the visibility data with five circular Gaussians accounts for almost all the flux density measured from the image.

Mrk 1218 (0835+250)

Y: Ulvestad (1986) found this object to be only slightly resolved at 5 GHz (VLA *A*-array) and 1.4 GHz (VLA *B*-array). Our map shows a diffuse, faint ($\sim 2\sigma$) extension toward the north-west in P.A. $\sim -45^\circ$. The total flux density of the source is dominated by the bright central component,

which is coincident with the optical nucleus (Clements 1983) within the errors. The total flux density of 25.5 mJy measured by us is consistent with the value of 23.0 mJy presented by (Ulvestad 1986). The spectral index derived from our 5 GHz observations and the 1.4 GHz observations of Ulvestad (1986) (obtained in February 1984) is $\alpha_{1.4\text{ GHz}}^{5\text{ GHz}} = 0.8$.

G: Apart from the brightest component (~ 7 mJy), we detect several blobs of fainter emission, some in the approximate direction of the kpc-scale elongation. Model-fitting the visibilities with four circular Gaussians accounts for most of the emission measured in the image plane by summing pixel values using the AIPS task IMEAN, and gives a total flux density approximately the same as that obtained by fitting Gaussians in the image plane using AIPS task JMFIT, *viz.*, 12 mJy.

NGC 2639 (0840+503)

Table 6. VLA observational results. ‡: The peak surface brightness of the radio image of NGC 5929 coincides with one of the hotspots and not the nucleus.

Object	Position of radio peak		optical-radio offsets		Peak surface brightness (mJy beam ⁻¹)	Component flux density (mJy)	Total	Largest angular size (arcsec)
	Right Ascension (J2000)	Declination	Δ RA (arcsec)	Δ Dec (arcsec)				
Mrk 1	01 ^h 16 ^m 07 ^s .209	+33°05'21".66	+0.61	-0.71	24.08	27.1	27.8	< 0.65
MCG 8-11-11	05 ^h 54 ^m 53 ^s .620	+46°26'21".41	-0.15	+0.20	23.57	65.3	78.0	3.48
NGC 2273	06 ^h 50 ^m 08 ^s .646	+60°50'44".94	+1.11	+0.07	12.13	14.3	22.0	2.25
	06 ^h 50 ^m 08 ^s .534	+60°50'45".08				6.3		
Mrk 78	07 ^h 42 ^m 41 ^s .724	+65°10'37".44	+0.09	+0.02	8.87	10.1	13.1	3.88
	07 ^h 42 ^m 41 ^s .340	+65°10'37".63				2.3		
Mrk 1218	08 ^h 38 ^m 10 ^s .945	+24°53'42".82	+0.08	+0.10	18.72	19.7	27.7	1.28
NGC 2639	08 ^h 43 ^m 38 ^s .072	+50°12'19".97	-0.08	+0.35	63.47	80.5	85.8	< 0.65
Mrk 766	12 ^h 18 ^m 26 ^s .517	+29°48'46".50	-0.11	+0.16	13.75	16.8	17.9	< 0.65
Mrk 477	14 ^h 40 ^m 38 ^s .097	+53°30'15".96	+0.20	+0.04	22.97	26.6	27.3	< 0.99
NGC 5929	15 ^h 26 ^m 06 ^s .113	+41°40'14".02‡	+0.30	+0.70	21.51	25.5	34.4	3.47
NGC 7212	22 ^h 07 ^m 01 ^s .998	+10°14'00".69	+0.18	-0.35	19.59	30.0	31.0	3.09
Ark 564	22 ^h 42 ^m 39 ^s .332	+29°43'31".07	+0.01	+0.24	8.62	10.7	11.4	< 0.85
NGC 7469	23 ^h 03 ^m 15 ^s .616	+08°52'26".02	+0.06	+0.37	21.97	26.9	47.9	2.76
Mrk 530	23 ^h 18 ^m 56 ^s .653	+00°14'37".96	-0.50	+0.27	8.02	8.3	10.2	< 0.82
Mrk 533	23 ^h 27 ^m 56 ^s .712	+08°46'44".13	+0.12	+0.40	38.19	60.4	58.8	1.89
NGC 7682	23 ^h 29 ^m 03 ^s .918	+03°31'59".92	+0.18	+0.07	21.98	22.3	22.6	< 0.94

Y: This much studied object is a triple (P.A. of -77°) with a bright central component (Ulvestad & Wilson 1989). Our map does not resolve the triple structure and, as in the map of Ulvestad & Wilson (1989), the radio peak lies to the south-east of the optical nucleus (Argyle & Eldridge 1990). This source is variable (A. Wilson, private communication). The integrated spectral index obtained using the observations of Thean et al. (2000) at 8.4 GHz (July 1995/November 1996 data) and of Ulvestad & Wilson (1989) at 5 GHz (February 1985 data), is $\alpha_{1.4 \text{ GHz}}^{5 \text{ GHz}} = 0.5$. The largest angular extent of the source as measured by Ulvestad & Wilson (1989) is ~ 1.7 arcsec. Ho et al. (1993) classify this source as a LINER.

G: Our map is dominated by the bright central component, with some weaker emission to the east (P.A. $\sim 90^\circ$), as is confirmed by our two-component model-fit. The main component contains almost $\sim 80\%$ of the total detected flux density. The flux density of the bright component 31.6 mJy ($1.8 \times 1.1 \text{ mas}^2$ beam size), is lower than the value of 47 mJy ($2.0 \times 1.7 \text{ mas}^2$ beam size) quoted by Wilson et al. (1998), but is higher than the flux density derived from the early VLBI measurements of Hummel et al. (1982), *viz.*, 27 mJy.

Mrk 766 (1215+300)

Y: This source is essentially unresolved in our map, but shows hints of a weak halo-like structure. The 5 GHz VLA A array image of Ulvestad & Wilson (1984a) shows it to be slightly resolved, with most of the extended emission lying slightly to the north of the bright component; they derive a linear size of ~ 100 pc. We detect a flux density of 15 mJy, similar to the 5 GHz flux density found by Ulvestad & Wilson (1984a). The radio peak and the optical nucleus (Clements 1981) are coincident within the errors. The spectral indices

derived using our observations along with the 8.4 GHz observations of Kukula et al. (1995) (obtained in June 1991) and the 1.5 GHz observations of Ulvestad & Wilson (1989) (obtained in February 1985) are $\alpha_{1.5 \text{ GHz}}^{5 \text{ GHz}} = 0.8$, and $\alpha_{5 \text{ GHz}}^{8.4 \text{ GHz}} = 1.1$.

G: Our slightly resolved image shows a slight extension towards the south (P.A. $\sim 160^\circ$), which we were not able to adequately model-fit; our model contains about 60 % of the total flux density on VLBI scales.

Mrk 477 (1439+537)

Y: Our image is essentially unresolved, whereas the image of Ulvestad & Wilson (1984a) at the same frequency and with similar resolution was slightly resolved. The central component in their map shows weak extensions in several different directions. Our total flux density is consistent with theirs within the errors, with $\sim 90\%$ of the total flux density being in the unresolved central component.

G: The object is dominated by a compact component containing about 80 % of the total flux density on VLBI scales, with some evidence for weak halo-like emission.

NGC 5929 (1524+418)

Y: The central component of the triple structure visible in the 8.4 GHz VLA A array image of Su et al. (1996) cannot be distinguished in our lower-resolution image. The spectral indices of the north-east and south-west components are steep, with $\alpha_{1.6 \text{ GHz}}^{15 \text{ GHz}} = 0.9$ and 0.8, respectively. The central component has a flatter spectrum, with $\alpha_{1.6 \text{ GHz}}^{15 \text{ GHz}} = 0.3$ (Su et al. 1996; Kukula et al. 1995; Wilson & Keel 1989) and is close to the position of the optical nucleus, and hence is likely to be the core. The epochs of these observations

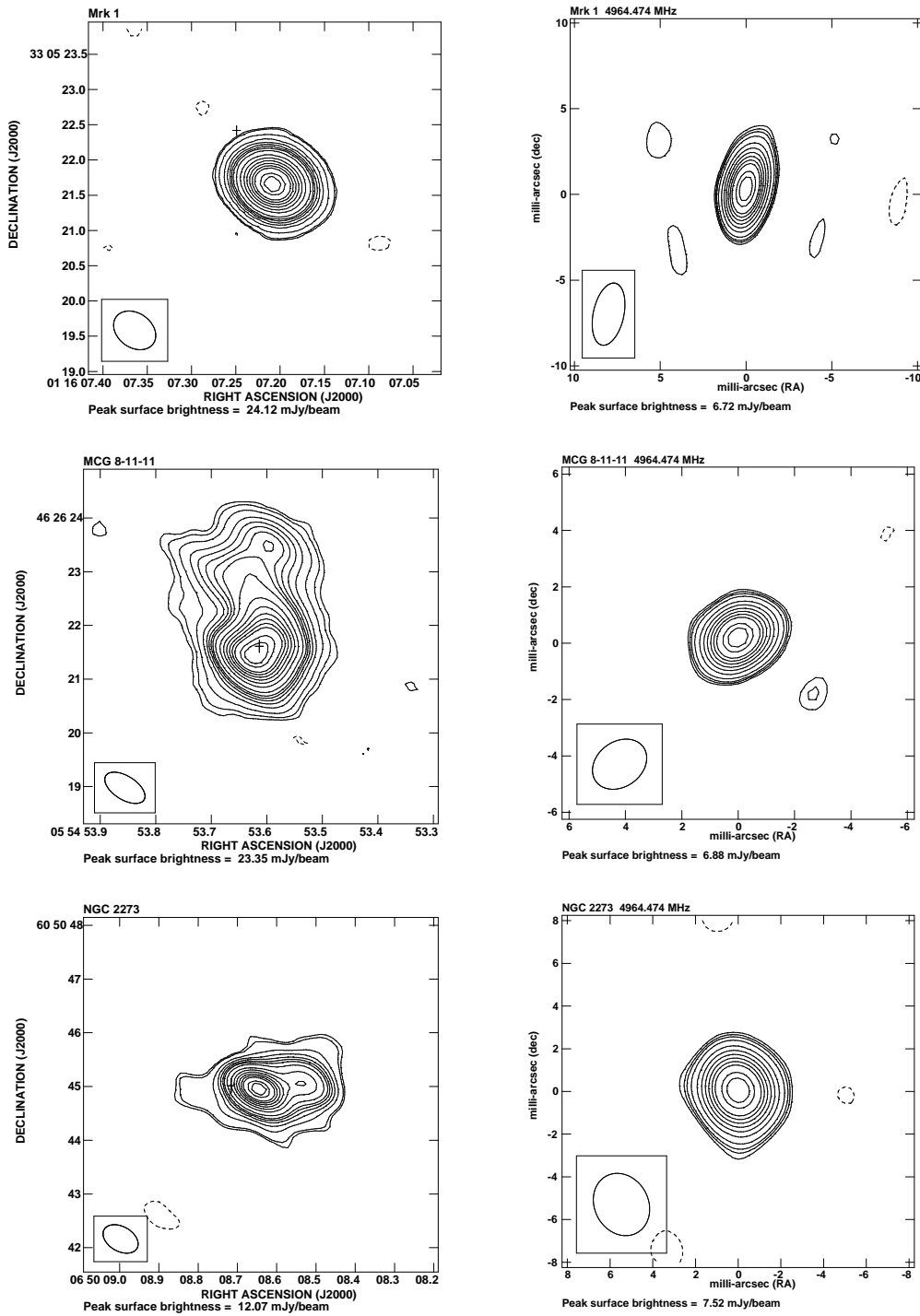


Fig. 1. The 5 GHz contour maps for all the targets, ordered in right ascension. The VLA and VLBI maps are in the left and right panels, respectively. The source name is given in the top left corner, and the boxed ellipse in the lower left-hand corner shows the shape of the FWHM synthesized beam in each case. A cross in the VLA maps marks the position of the optical nucleus, with the size of the cross representing the uncertainty in the position. All positions are given in J2000 coordinates. The contour levels and surface brightness peaks are listed in Tables 3 (VLA maps) and 4 (VLBI maps)

are August 1993 (1.6 GHz), November 1992 (5 GHz), June 1990 (8.4 GHz) and March 1989 (15 GHz). We also detect 8 mJy from the unresolved neighboring galaxy NGC 5930 (Fig. 2, left panel), as is reported by Kukula *et al.* (1995) for

VLA *C* configuration data at 8.4 GHz. The largest angular size of the source is ~ 2.0 arcsec (Kukula *et al.* 1995). *G*: Our image shows a compact source with some signs of weak extensions toward the east or north-east, along

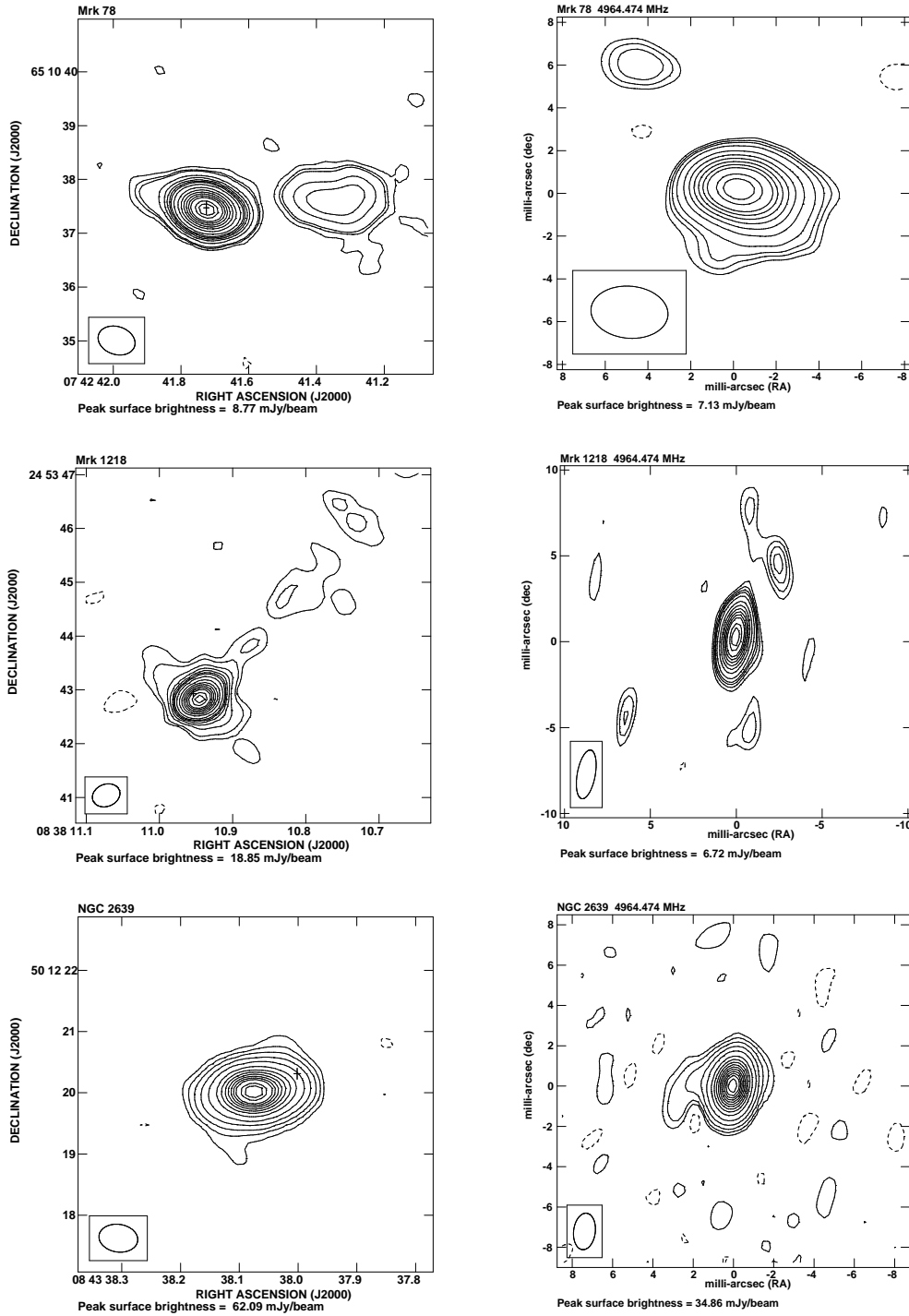


Fig. 1. (continued).

P.A. $\sim 50^\circ$. A possible weak component found in our model-fitting is located to the north-east (~ 3 mas) of the bright component. Using the VLA core spectral index, $\alpha_{15\text{ GHz}}^{1.6\text{ GHz}} \simeq 0.32$ (Su et al. 1996), the core should have flux density of 1.1 mJy at 5.0 GHz. We detect a total flux density of 6.8 mJy in our VLBI image, and therefore conclude that the detected mas-scale component corresponds to one of the two steep spectrum components of the triple (Su et al. 1996), and not to the core. We have tried to map a larger

field to image the second steep-spectrum component, but were not able to detect it. It is possible that this second component is resolved out by our VLBI data; however, given that the spacing between the two components is ~ 1.3 arcsec (Su et al. 1996), it is likely that the variations in the visibilities would be too rapid to be tracked with the (u, v) and time coverage of our data. Thus, we feel that our data do not rule out the presence of a second compact component coincident with the distant steep-spectrum lobe.

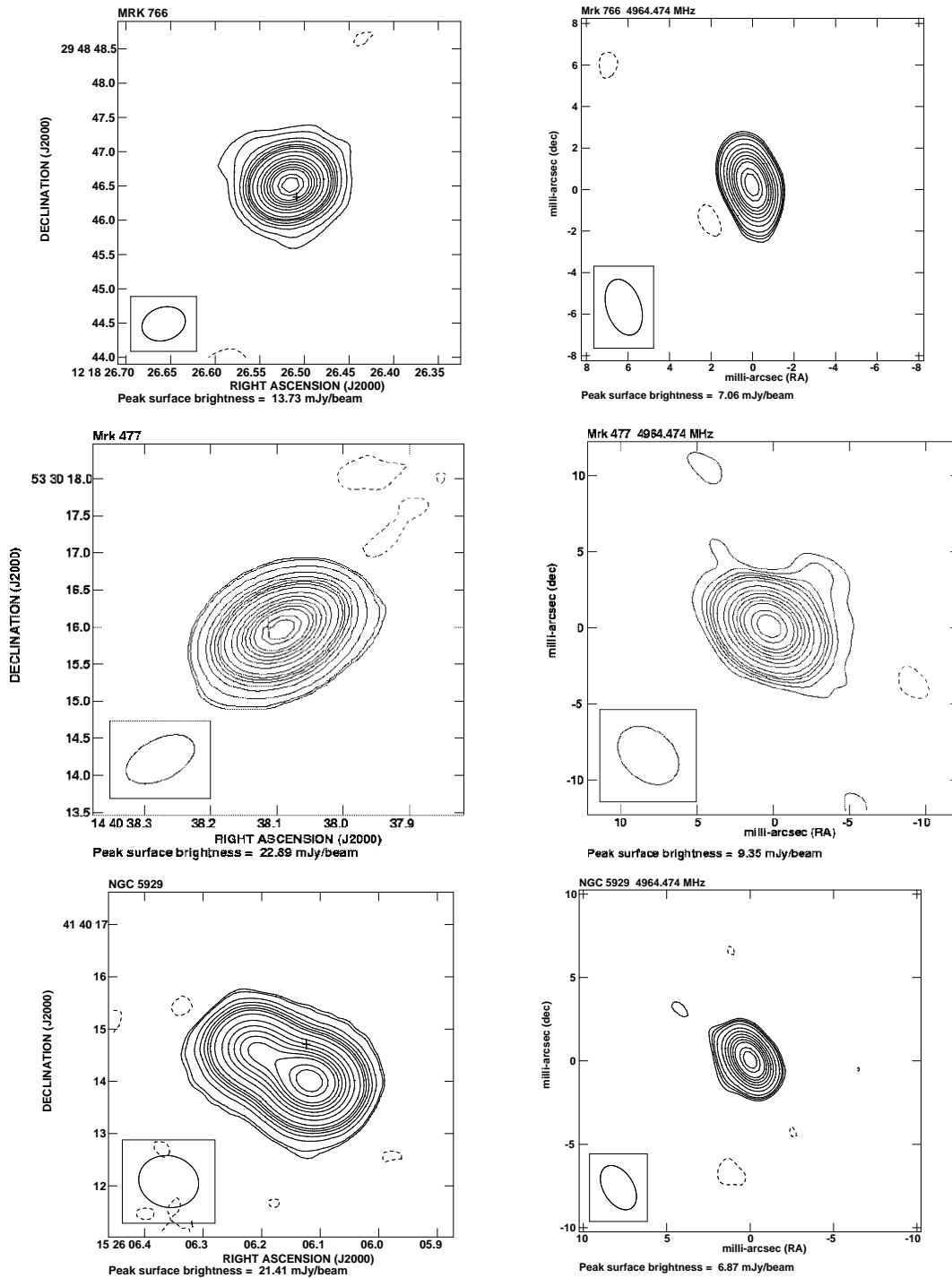


Fig. 1. (continued).

NGC 7212 (2204+095)

Y: Our map does not resolve the compact double separated by 0.7 arcsec to the north-west as clearly as the 8.4 GHz, VLA *A* array map of Falcke *et al.* (1998). However, our map does show an obvious extension towards the north (P.A. $\sim 10^\circ$), as well as fainter extensions roughly to the south and south-east. The largest angular size of the source is ~ 3 arcsec. We note that the position of the phase cal-

ibrator that we used was in error at the time of our observations, but has since been updated by the NRAO; we have incorporated this correction in our image using the AIPS task OGEOM. NGC 7212 is in an interacting system (Wasilewski 1981) and we detect faint radio emission from its closest companion, seen $\sim 14''$ to its north-east (Fig. 2, right panel). The companion is visible in the Digital Sky Survey images and is clearly delineated in the 2MASS images.

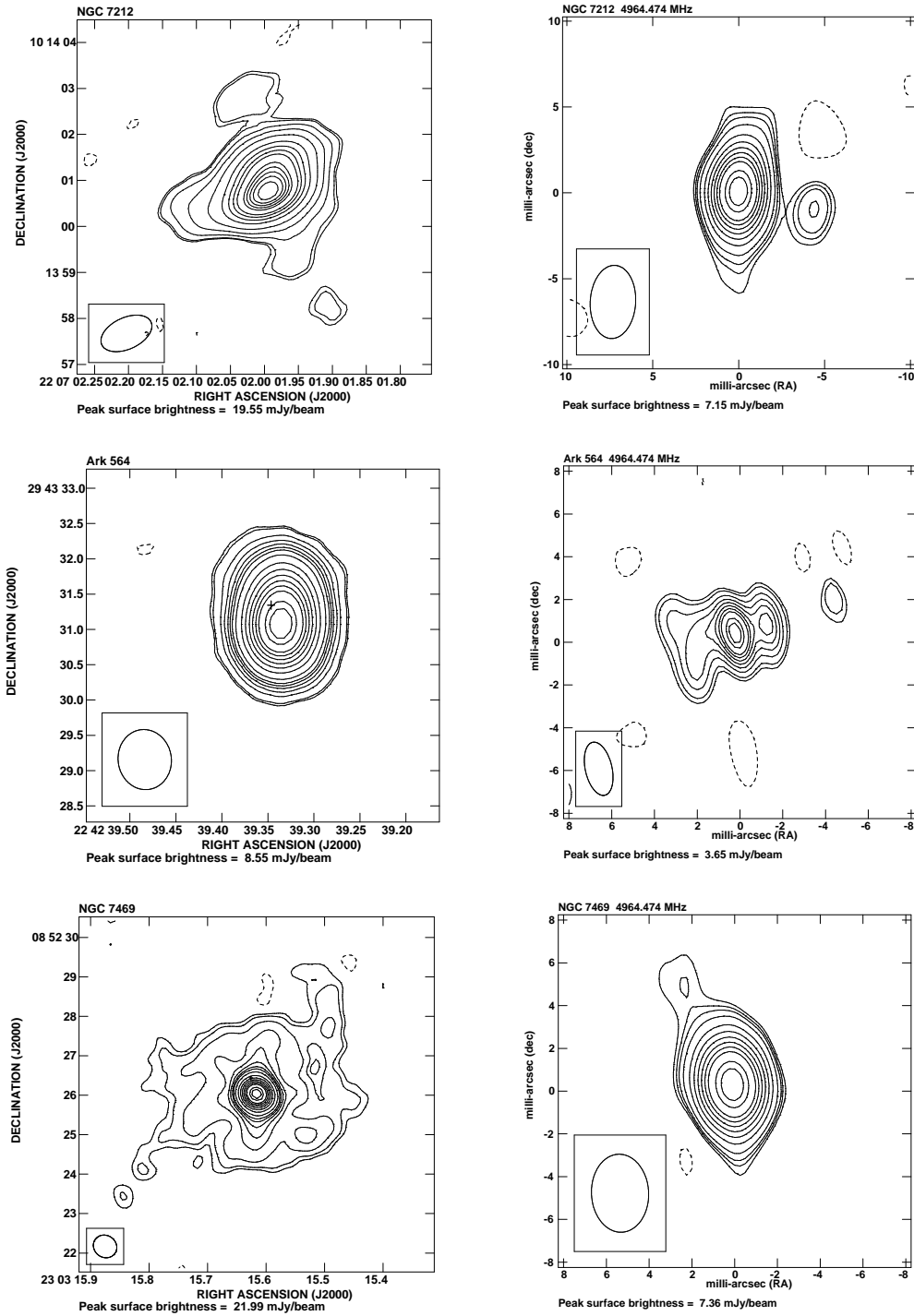


Fig. 1. (continued).

G: Apart from the bright primary component, we detect a secondary nearly to the west (P.A. $\sim -110^\circ$), as well as an extension toward the north, roughly in the direction of the arcsecond-scale structure. About 90 % of the total VLBI-scale flux density is contained in our two-component model.

Ark 564 (2240+294)

Y: Although our map does not clearly resolve the triple structure extending to 320 pc in P.A. = 6° seen by Schmitt et al. (2001) (8.4 GHz, VLA A array), it is extended in the direction of this structure. Our radio peak coincides with the optical nucleus (Clements 1981) within the errors. The total flux density at 5 GHz is the same as that quoted by Ulvestad et al. (1981) within the errors.

G: This is the faintest source in our sample and was detected on the least number of baselines. Accordingly, the (u, v)

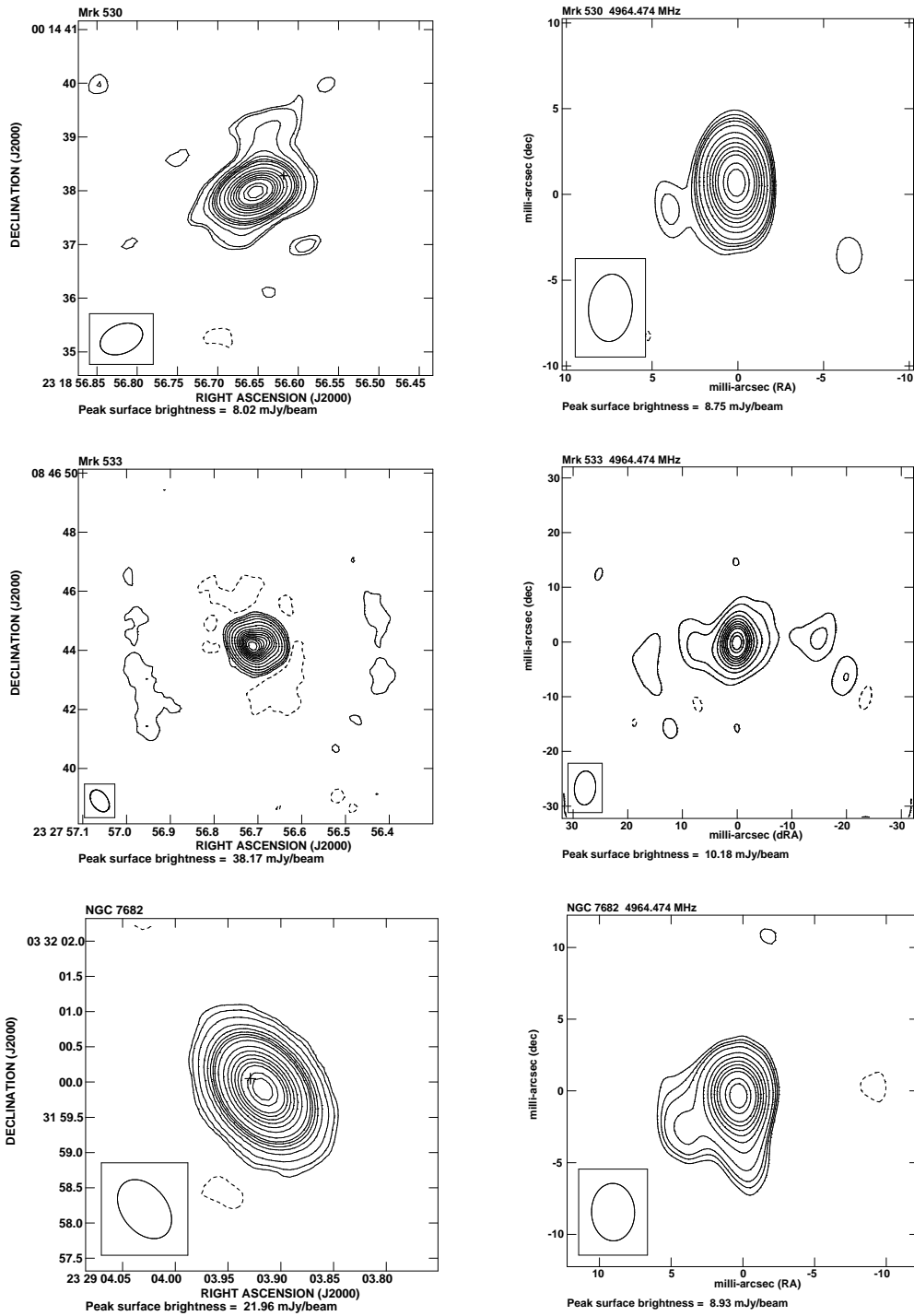


Fig. 1. (continued).

coverage obtained was relatively poor. Although our map shows an elongated structure with four components in P.A. $\sim 110^\circ$, we do not feel confident that this is an accurate representation of the VLBI-scale structure of the source. Attempts to model-fit this structure were not successful, and so our single-component fit has essentially fit the parameters of the brightest component. The inadequacy of the fit as a description of the VLBI-scale emission as a whole is

reflected in the fact that only 35 % of the total VLBI-scale flux density is reproduced by the model.

NGC 7469 (2300+086)

Y: Our image shows a halo ~ 4 kpc in extent around the dominant compact component, which is coincident with the optical nucleus (Clements 1981), similar to the images in Wilson et al. (1991). Wilson et al. (1991) determine the spectral index to be $\alpha_{5\text{ GHz}}^{15\text{ GHz}} \sim 0.9$. The features seen

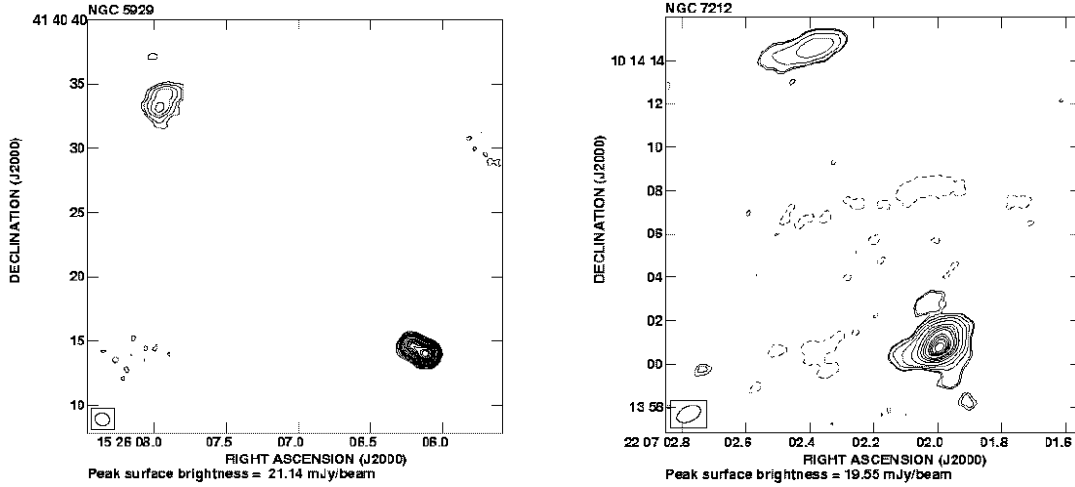


Fig. 2. Left panel shows a large VLA map of NGC 5929 including NGC 5930. Right panel shows a large VLA map of NGC 7212 including the emission detected from its companion to the north-east.

in this source are also seen by Condon et al. (1982) and Ulvestad et al. (1981) in their lower resolution images. The 8.4 GHz map presented by Kukula et al. (1995) also shows a point source surrounded by faint emission. Using our flux density and that given by Kukula et al. (1995) at 8.4 GHz (obtained in June 1991), we obtain the integrated spectral index $\alpha_{5\text{ GHz}}^{8.4\text{ GHz}} = 0.9$, similar to the $\alpha_{5\text{ GHz}}^{15\text{ GHz}}$ value determined by Wilson et al. (1991).

G: Most of the detected emission is from a compact component, though there appears to be an extension toward the north-east. This is consistent with the prediction of Smith et al. (1998), who, based on their observed visibility functions, suggested the presence of multiple components. Using our detected flux density and the 1.4 GHz correlated flux density measured by Smith et al. (1998) of 12 mJy (September 1991), we obtain the spectral index $\alpha_{1.4\text{ GHz}}^{5\text{ GHz}} = 0.5$.

Mrk 530 (2316–000)

Y: This source was reported to be a compact point source by Kukula et al. (1995) at 8.4 GHz, whereas our 5 GHz map shows a compact source and a faint (3σ) extension to the north (P.A. $\sim -10^\circ$). Comparing our total flux density with the 3.26 mJy found by Kukula et al. (1995) at 8.4 GHz in June 1991, we derive the spectral index $\alpha_{5\text{ GHz}}^{8.4\text{ GHz}} = 2$. Our total flux density is consistent with the measurements of Edelson (1987) (11.5 mJy), and Roy et al. (1994), *viz.*, a correlated flux density of 11 mJy obtained using a single 275 km baseline at 2.3 GHz.

G: Our model-fitting suggests that, in addition to the faint extension to the south-east seen in the map, the compact core also has an extension ~ 1.9 mas to the south-west. The total flux density is similar to the flux density associated with the central component in the arcsec-scale image. This implies that almost all of the radio emission detected on arcsec-scale image is associated with this compact component.

Mrk 533 (2325+085)

Y: Our image is consistent with the image of Momjian et al. (2003), the double structure seen in the 8.4 GHz VLA A configuration map of Kukula et al. (1995) and the 1.6 GHz MERLIN map of Unger et al. (1986). The structural P.A. is $\sim -60^\circ$. The peak of the brightest radio component (component ‘C’ of Momjian et al. (2003)) is ~ 0.4 arcsec to the south of the optical position of Clements (1983).

G: On mas-scales, we detect only component ‘C’ of Momjian et al. (2003), which forms a linear radio source extending in the east-west direction. Our model-fitting indicates the presence of five components. The CLEAN components are distributed out to ~ 15 mas on either side of the phase centre (total extent of ~ 30 mas) along P.A. $\sim -80^\circ$, similar to the P.A. of the arcsec-scale radio structure ($\sim -60^\circ$). Our model contains about 80 % of the total flux density that we detect on VLBI scales.

NGC 7682 (2326+032)

Y: Our map is unresolved, as was also true of the image of Kukula et al. (1995). Combining our flux density with the 8.4 GHz flux density given by Kukula et al. (1995) (obtained in June 1991) yields a spectral index $\alpha_{5\text{ GHz}}^{8.4\text{ GHz}} \simeq 1.1$. The radio peak coincides with the optical nucleus (Clements 1983) within the errors.

G: The image shows clear evidence for extended structure to the south (P.A. $\sim 180^\circ$) and south-east (P.A. $\sim 120^\circ$). The best model-fit to the visibilities was a combination of one circular Gaussian and two point sources which accounts for most (about 80 %) of this emission.

5. Conclusions

We have detected all the 15 Seyferts that we observed with VLBI. We have presented here the VLBI images and simultaneous VLA images that we obtained.

In $\sim 30\%$ of the cases, we detect a single component on mas-scales. In 40 % of the cases, at least half of the total emission on arcsec scales is detected in the VLBI images. In

Mrk 530, almost all the emission from the arcsec-scale core is present on mas-scales. The measurements presented here represent most of the database that we require for rigorously testing the predictions of the US for Seyferts with respect to their parsec-scale radio structure. We will present the results of such tests in an accompanying paper.

Acknowledgements. Our many thanks to the support staff of the European VLBI Network and the National Radio Astronomy Observatory, and especially to Joan Wrobel and Craig Walker for help in scheduling the VLBI observations. We also thank the referee, Dr. Alan Roy, for his prompt review of the manuscript, and for useful and detailed comments that lead to improvement of the paper.

This project was done with financial support from the Indo-Russian International Long Term Programme of the Department of Science and Technology, Government of India and the Russian Academy of Sciences. Financial support in the initial phase from the Indian National Science Academy exchange programme is also acknowledged. DVL acknowledges support from the Joint Institute for VLBI in Europe for a visit there. DG acknowledges support from the European Commission under TMR contract No. ECBFMGECT950012. The VLA and VLBA are operated by the National Radio Astronomy Observatory, a facility of the National Science Foundation operated under cooperative agreement by Associated Universities, Inc. The European VLBI Network is a joint facility of European, Chinese and other radio astronomy institutes funded by their national research councils. This research has made use of NASA's Astrophysics Data System bibliographic services, the NASA/IPAC Extragalactic Database (NED) which is operated by the Jet Propulsion Laboratory, California Institute of Technology, under contract with NASA, and the SIMBAD database, operated by CDS, Strasbourg, France.

References

- Antonucci, R. 1993, *ARA&A*, 31, 473
 Antonucci, R. R. J. & Miller, J. S. 1985, *ApJ*, 297, 621
 Argyle, R. W. & Eldridge, P. 1990, *MNRAS*, 243, 504
 Baum, S. A., O'Dea, C. P., Dallacasa, D., de Bruyn, A. G., & Pedlar, A. 1993, *ApJ*, 419, 553
 Cid Fernandes, R. 1997, in *Revista Mexicana de Astronomia y Astrofisica Conference Series*, Vol. 6, 201
 Clements, E. D. 1981, *MNRAS*, 197, 829
 —. 1983, *MNRAS*, 204, 811
 Condon, J. J., Condon, M. A., Gisler, G., & Puschell, J. J. 1982, *ApJ*, 252, 102
 Edelson, R. A. 1987, *ApJ*, 313, 651
 Falcke, H., Wilson, A. S., & Simpson, C. 1998, *ApJ*, 502, 199
 Gabuzda, D. C. 1988, PhD thesis, Brandeis University, U.S.A.
 Gallouët, L., Heidmann, N., & Dampierre, F. 1975, *A&AS*, 19, 1
 Ho, L. C., Filippenko, A. V., & Sargent, W. L. W. 1993, *ApJ*, 417, 63
 Hummel, E., Fanti, C., Parma, P., & Schilizzi, R. T. 1982, *A&A*, 114, 400
 Khachikian, E. Y. & Weedman, D. W. 1974, *ApJ*, 192, 581
 Kukula, M. J., Ghosh, T., Pedlar, A., & Schilizzi, R. T. 1999, *ApJ*, 518, 117
 Kukula, M. J., Pedlar, A., Baum, S. A., & O'Dea, C. P. 1995, *MNRAS*, 276, 1262
 Momjian, E., Romney, J. D., Carilli, C. L., & Troland, T. H. 2003, *ApJ*, 597, 809
 Moran, E. C., Barth, A. J., Kay, L. E., & Filippenko, A. V. 2000, *ApJ*, 540, L73
 Nagar, N. M., Wilson, A. S., Mulchaey, J. S., & Gallimore, J. F. 1999, *ApJS*, 120, 209
 Osterbrock, D. E. 1989, *Astrophysics of Gaseous Nebulae and Active Galactic Nuclei* (Mill Valley, California, USA: University Science Books)
 Pier, E. A. & Krolik, J. H. 1993, *ApJ*, 418, 673
 Roy, A. L., Norris, R. P., Kesteven, M. J., Troup, E. R., & Reynolds, J. E. 1994, *ApJ*, 432, 496
 Schmitt, H. R., Ulvestad, J. S., Antonucci, R. R. J., & Kinney, A. L. 2001, *ApJS*, 132, 199
 Shastri, P., Lal, D. V., & Gabuzda, D. C. 2003, in *ASP Conf. Ser. 290: Active Galactic Nuclei: From Central Engine to Host Galaxy*, 311
 Smith, H. E., Lonsdale, C. J., & Lonsdale, C. J. 1998, *ApJ*, 492, 137
 Sramek, R. A. & Tovmassian, H. M. 1975, *ApJ*, 196, 339
 Su, B. M., Muxlow, T. W. B., Pedlar, A., et al. 1996, *MNRAS*, 279, 1111
 Thean, A., Pedlar, A., Kukula, M. J., Baum, S. A., & O'Dea, C. P. 2000, *MNRAS*, 314, 573
 Ulvestad, J. S. 1986, *ApJ*, 310, 136
 Ulvestad, J. S. & Wilson, A. S. 1984a, *ApJ*, 278, 544
 —. 1984b, *ApJ*, 285, 439
 —. 1986, *MNRAS*, 218, 711
 —. 1989, *ApJ*, 343, 659
 Ulvestad, J. S., Wilson, A. S., & Sramek, R. A. 1981, *ApJ*, 247, 419
 Unger, S. W., Pedlar, A., Booler, R. V., & Harrison, B. A. 1986, *MNRAS*, 219, 387
 Walker, C. 2003, *The SCHED User Manual*, <http://www.aoc.nrao.edu/~cwalker/sched/sched/sched.html>
 Wasilewski, A. J. 1981, *PASP*, 93, 560
 Wilson, A. S., Helfer, T. T., Haniff, C. A., & Ward, M. J. 1991, *ApJ*, 381, 79
 Wilson, A. S. & Keel, W. C. 1989, *AJ*, 98, 1581
 Wilson, A. S., Roy, A. L., Ulvestad, J. S., et al. 1998, *ApJ*, 505, 587